Applied Surface Science 649 (2024) 159189

Contents lists available at ScienceDirect

Applied Surface Science

journal homepage: www.elsevier.com/locate/apsusc

Full Length Article

Wide-field surface plasmon resonance microscope based on polyethylene oxide/polyacrylic acid brushes

Qais M. Al-Bataineh [a,b,*], Ahmad D. Telfah [c,d], Carlos J. Tavares [e], Roland Hergenröder [a,*]

[a] Leibniz-Institut für Analytische Wissenschaften-ISAS-e.V., 44139 Dortmund, Germany
[b] Department of Physics, TU Dortmund University, 44227 Dortmund, Germany
[c] Nanotechnology Center, The University of Jordan, 11942 Amman, Jordan
[d] Department of Physics, University of Nebraska at Omaha, Omaha NE-68182, USA
[e] Physics Centre of Minho and Porto Universities (CF-UM-UP), University of Minho, 4804-533 Guimaraes, Portugal

ARTICLE INFO

Keywords:
Surface plasmon resonance (SPR)
Imaging wide-field SPR microscope (WF-SPRM)
Polyelectrolyte brushes (PEBs)
Polyacrylic acid (PAA)
Polyethylene oxide (PEO)

ABSTRACT

Wide-field surface plasmon resonance microscope (WF-SPRM) based on polyethylene oxide/polyacrylic acid (PEO/PAA) polyelectrolyte brushes (PEBs) is presented for particle detection application. PEO acts as an H-bond acceptor, while PAA serves as an H-bond donor, forming hydrogen-bonding complexes within the brushes. Morphological, chemical, and crystal structural analyses confirm that the PEO/PAA brushes undergo a transition from a collapsed to a stretched state as the solvent pH is increased from 1 to 10. This pH-dependent change also renders the PEO/PAA brushes more hydrophilic. Additionally, the electrical conductivity and refractive index of the PEO/PAA brushes increase concomitantly with the increase of solvent pH. Furthermore, theoretical and experimental approaches study the sensitivity of WF-SPRM utilizing Au-(PEO/PAA) polyelectrolyte layers. The theoretical sensitivity of WF-SPRM is enhanced from 118.5 deg./RIU for the Au-layer to 178.1 deg./RIU for Au-(PEO/PAA PEBs). Moreover, the signal-to-noise ratio for the Au-(PEO/PAA PEBs) layer is 20 ± 1, indicating improved sensing performance compared to the Au-layer (signal-to-noise ratio of 6 ± 1). A mathematical model to describe the discrete particle detection by WF-SPRM is presented, where results demonstrate a good agreement between the calculated intensity profile and experimental data.

1. Introduction

Polyelectrolyte brushes (PEBs) are a class of intelligent polymers with the remarkable ability to undergo reversible transformations between different shapes when exposed to external stimuli, such as changes in pH, light, temperature, or electric fields [1]. The versatility of PEBs makes them highly promising for various practical applications, including sensors, smart actuators, and biomedical devices [2–5]. The formation of polymer–polymer complexes arises from noncovalent interactions between the functional groups of the polymer chains [6]. These complexes can be further categorized based on the dominating interaction types, such as polyelectrolyte complexes driven by Coulombic forces, hydrogen-bonding complexes stabilized by hydrogen bonds, and charge-transfer complexes [7,8].

This study focuses on investigating the polymer–polymer complexes formed by polyethylene oxide (PEO) and polyacrylic acid (PAA), which are classified as hydrogen-bonding complexes. PEO possesses H-bond acceptor properties, enabling the formation of hydrogen-bonding complexes [9]. Moreover, PEO-based hydrogen-bonding complexes can be created with H-bond donor polymers like polyelectrolytes [10,11]. Among the polyelectrolytes, PAA is a weak polyelectrolyte brushes (PEBs) containing carboxylic acid, exhibiting variations in structures, charges, and hydrophilicity at different pH levels [12,13]. PAA PEBs have diverse applications, including protein refinement, enzyme immobilization, drug delivery, bioinspired nanoreactors, artificial joints, smart actuators, and bioelectronic devices [14–16].

Mixed PEBs, combining protein-adsorbing and protein-repellent properties, can be beneficial for protein adsorption and nano-particle detection [17]. Previous models based on PEO/PAA brushes in saline solutions suggested that PEO/PAA brushes efficiently adsorb and desorb proteins [18,19]. The physical interactions between PEBs and macromolecules remain a topic of investigation, with proposed mechanisms involving local patches on the macromolecule surface and the environment within the PEBs [20–23].

* Corresponding authors at: Leibniz Institut für Analytische Wissenschaften-ISAS-e.V., 44139 Dortmund, Germany (Q.M. Al-Bataineh).
E-mail addresses: qais.albataineh@tu-dortmund.de (Q.M. Al-Bataineh), a.telfah@ju.edu.jo (A.D. Telfah), roland.hergenroeder@isas.de (R. Hergenröder).

https://doi.org/10.1016/j.apsusc.2023.159189
Received 6 November 2023; Received in revised form 12 December 2023; Accepted 19 December 2023
Available online 21 December 2023

To enhance surface plasmon resonance (SPR) sensitivity, a wide-field surface plasmon resonance microscope (WF-SPRM) based on Au-(PEO/PAA PEBs) layers is designed. WF-SPRM is a spatiotemporal sensor capable of imaging nano-objects in solution through interactions with the sensor surface [24,25]. This sensor can detect individual nano-objects, such as viruses and virus-like particles [26,27].

The presented work investigates the chemical, crystal, and morphological properties of switchable PEO/PAA PEBs under varying pH conditions. An increase in pH value transforms the carboxylic acid (COOH) groups into carboxylate (COO^-) groups, leading to the transformation of collapsed PEBs into stretched PEBs. Additionally, the effect of pH variation on the optical refractive index, electrical conductivity, and hydrophobicity behavior of the PEO/PAA PEBs is explored.

2. Experimental sections

2.1. Synthesis technique

The "grafting to" method was employed for depositing PEO/PAA PEBs through thiol group modification. Initially, stock solutions of polyethylene oxide (PEO, 300,000 $g.mol^{-1}$, Sigma-Aldrich) and polyacrylic acid (PAA, 1800 $g.mol^{-1}$, Sigma-Aldrich) were prepared by dissolving 1.0 g of each polymer in 100 mL distilled water under continuous stirring at 45 °C for five hours. Subsequently, a PEO/PAA blend (50:50 wt%) stock solution was formed using the solution mixing method and subjected to sonication at 40 °C for five hours to produce PEO/PAA blends.

Thiolated PEO/PAA (PEO/PAA-SH) was then prepared by performing carbodiimide amide coupling reactions for one in four hydroxyls and/or carboxylic acid groups, following previous research [28]. In which 0.320 g of N-hydroxy succinimide (115.09 $g.mol^{-1}$, Sigma-Aldrich) and 0.533 g of 1-ethyl-3-(3-(dimethylamino) propyl) carbodiimide) hydrochloride (155.245 $g.mol^{-1}$, Sigma-Aldrich) were added into 100 mL of PEO/PAA stock solution under continuous stirring for 30 min at room temperature. After that, 0.316 g of cysteamine hydrochloride (113.61 $g.mol^{-1}$, Sigma-Aldrich) was added to the reaction under continuous stirring for four hours at room temperature. Finally, the PEO/PAA-SH PEBs were purified by adding toluene in small amounts to the final solution. The initial solution had a pH value of approximately 1, which was adjusted to 4, 7, and 10 by adding sodium hydroxide (NaOH, 39.997 g/mol, Sigma-Aldrich) to the PEO/PAA-SH solvent.

Before surface functionalization, n-type silicon wafers and ITO glass substrates were cleaned using acetone for 30 min in a sonication bath. Gold substrates, consisting of a 5 nm adhesion Ti-layer and approximately 41–45 nm Au-layer on glass, were cleaned using piranha solution for 10 min. All substrates were then rinsed with distilled water and dried using argon gas. The PEO/PAA-SH PEBs with about 20 nm were deposited onto the substrates using the spin coating method. Finally, the films were dried at 70 °C under ambient pressure to evaporate the solvents. The "grafting to" method is illustrated in Figure S1.

2.2. Characterization techniques

The chemical structure analysis of the polyelectrolyte brushes was carried out using three main spectroscopic techniques: Fourier-transform infrared spectroscopy (FTIR) (Bruker VERTEX 80/80v Vacuum FTIR Spectrometers), nuclear magnetic resonance (^1H NMR) (Bruker AVANCE III NMR spectrometer, 600.13 MHz, 600 μL D_2O: 200 μL PEO/PAA-SH solution), and near-ambient pressure X-ray photoelectron spectroscopy NAP-XPS (SPECS Surface Nano Analysis GmbH). In parallel, the crystal structure investigation of the PEBs was conducted using an X-ray diffractometer (Malvern Panalytical Ltd) with Cuk_α radiation. For assessing the morphological properties of the PEBs, atomic force microscopy (AFM) (SPM SmartSPM™-1000) and water contact angle experiments have recurred. The refractive index was determined based on the optical properties measured using a UV–Vis spectrophotometer (Hitachi U-3900H), following the procedures already outlined [28–30]. Electrical conductivity measurements were carried out using a 4-point probe (Microworld Inc.).

Additionally, WF-SPRM measurements were performed as previously described [28,31]. The PEO/PAA-SH PEBs at pH 7 were deposited on a gold substrate by spin-coating technique, resulting in a thickness of ~20 nm. Silica nanoparticles (refractive index n = 1.420 [32]) with an average size of 100 nm were employed to Simulate biological particles due to their refractive index similarity to biological particles.

3. Results and discussion

PEO/PAA blend PEBs with a weight ratio of 50:50 were synthesized using the solution mixing method. These blends form interpolymer hydrogen bonds, with the ether oxygen atoms in PEO acting as H-acceptors and the carboxylate group of PAA acting as H-donors (Supplementary S2) [1]. However, applying PEO/PAA PEBs as coatings on various substrates poses a challenge due to the absence of strongly functional group binding to the surfaces. To address this, thiol groups were introduced into the hydroxyl and carboxylic groups of PEO/PAA PEBs through carbodiimide amide coupling reactions (Supplementary S3).

3.1. Dissociation behavior of PEO/PAA PEBs

The dissociation behavior of PEO/PAA PEBs was investigated using FTIR spectroscopy, as the COOH and COO^- groups exhibit distinct vibrational bands at different IR wavelengths [33]. Fig. 1a presents the vibrational bands of COOH and COO^- groups in PEO/PAA PEBs at varying pH values (1, 4, 7, and 10). At pH equal to 1, the vibrational band of COOH groups (at approximately 1700 cm^{-1}) is about 7 times higher than the vibrational band of asymmetric COO^- groups (at around 1500 cm^{-1}), with no observable symmetric COO^- groups. As the pH value increases to 4, the vibrational band of COOH groups decreases, while the vibrational bands of symmetric and asymmetric COO^- groups increase due to the dissociation of COOH groups by OH^- ions. However, the vibrational band of COOH groups remains approximately 3 times more intense than the combined vibrational bands of symmetric and asymmetric COO^- groups. Further elevation of the pH value to 10 results in the dominance of symmetric and asymmetric COO^- groups, leading to increased electrostatic repulsion within the polymer chains and elongation of the brushes. The dissociation degree at each pH value was calculated using methods from the literature [34]. Plotting the dissociation degree against the solvent pH values yields the titration curve of the PEO/PAA PEBs (Fig. 1b), which was fitted to the sigmoid function [34]. The effective dissociation constant (pKa) of the PEO/PAA PEBs is 4.95.

Fig. 1c displays the ^1H NMR spectra of PEO/PAA PEBs at different pH values. The signals observed at 1.10, 1.0–1.7, and 2.32 ppm correspond to CH_3, CH_2, and CHCOOH protons, respectively, in the PAA segments. The broad peak at 3.62 ppm is attributed to $-OCH_2CH_2-$ in the PEO segments. With an increase in pH from 1 to 10, the CHCOOH signal shifts to lower chemical shifts, indicating a transformation to $CHCOO^-$, leading to electrostatic repulsion between the brushes. The surface morphology of the PEO/PAA PEBs is affected by the solvent pH values, as evidenced by AFM measurements at pH values of 1, 4, 7, and 10 (Fig. 2). At low pH values (1 and 4), the dominance of COOH groups results in collapsed brushes, indicating the absence of repulsion forces between the brushes, with surface roughness about 1 nm and 3 nm, and thickness about 17 nm and 19 nm, respectively (Fig. 2a and 2b). As the pH increases to 7, the COOH groups dissociate into negatively charged COO^- groups, inducing electrostatic repulsion between the brushes and transforming them into swollen brushes, with surface roughness of 5 nm and thickness of 20 nm (Fig. 2c). At pH 10, complete dissociation of COOH groups to COO^- groups intensify the electrostatic repulsion

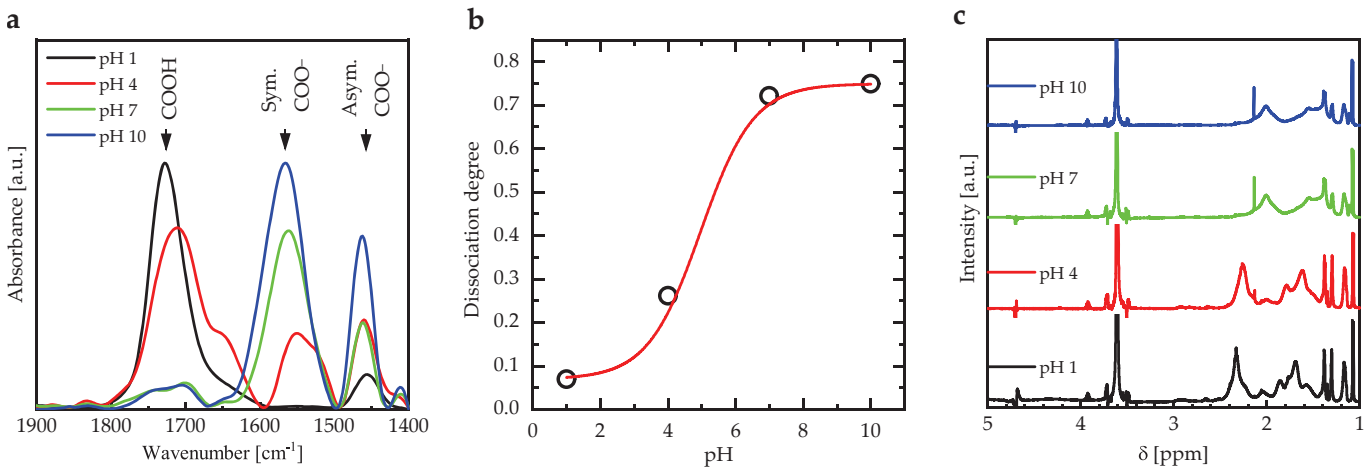

Fig. 1. **(a)** Fourier Transform Infrared (FTIR) spectra of PEO/PAA PEBs at pH values of 1, 4, 7, and 10 within the wavenumber range of 1400–1900 cm^{-1}. **(b)** Plot illustrating the dissociation degree of PEO/PAA PEBs as a function of pH value. **(c)** ^{1}H NMR) spectra of PEO/PAA PEBs recorded at pH values of 1, 4, 7, and 10.

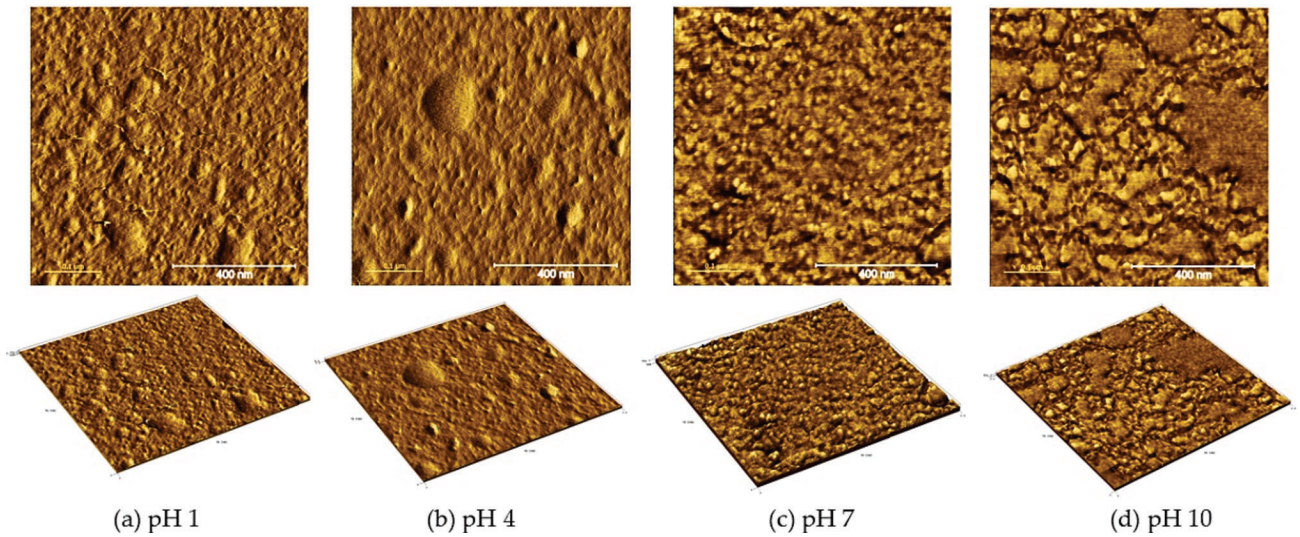

Fig. 2. 2D- and 3D-AFM micrographs of PEO/PAA PEBs at different pH values, namely **(a)** pH 1, (b) pH 4, **(c)** pH 7, and **(d)** pH 10.

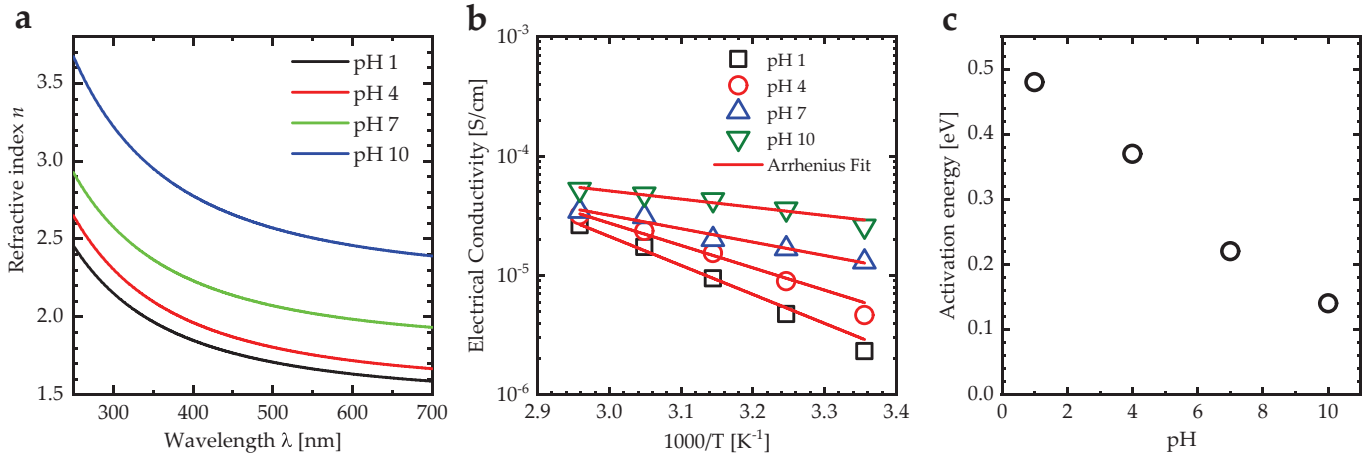

Fig. 3. **(a)** Refractive index spectra of PEO/PAA PEBs at various pH values. **(b)** Electrical conductivity of PEO/PAA PEBs at different pH values as a function of 1000/T $[K^{-1}]$. **(c)** The activation energy of the PEO/PAA PEBs as a function of pH value.

between the brushes, leading to stretched brushes with surface roughness of 7 nm and thickness of 23 nm (Fig. 2d). Moreover, higher pH values (pH 7 and 10) promote increased hydrophilicity of PEO/PAA PEBs, enhancing interacting surfaces between the PEBs and the surrounding medium (Supplementary S4). Additionally, as pH values increase to 10, the crystallinity degree of PEO/PAA PEBs changes due to the forming of new PEBs from a collapsed to a stretched state (Supplementary S5).

3.2. Optical and electrical properties

The sensitivity of SPR in the WF-SPRM relies on the refractive index (n) of the dielectric layer that coats the Au layer. Thus, the refractive index spectra of PEO/PAA PEBs for various solvent pH values are investigated (Fig. 3a). At pH 1, the refractive index of PEO/PAA PEBs decreases from 2.45 to 1.59 as the incident photon wavelength increases from 250 to 700 nm, being 1.59 at 685 nm. As the pH values increase to 10, n increases continuously, reaching 2.40 at 685 nm, which is attributed to the transformation of PEBs from collapsed brushes to stretched brushes. However, particle detection by WF-SPRM was performed at pH 7. At pH 7, *the* refractive index of PEO/PAA PEBs decreases from 2.93 to 1.93 in the range of 250 to 700 nm, being 1.94 at 685 nm.

Furthermore, the electrical conductivity (σ) of the PEO/PAA PEBs increases with increasing solvent pH, attributed to the dissociation of COOH groups into negatively charged COO^- groups, enhancing the ion transfer inside the polymer brush and consequently increasing electrical conductivity [33]. An increase in temperature also leads to increased electrical conductivity due to higher segment vibration energy, resulting in more segmental motion and enhanced ion mobility [35,36]. The electrical conductivity of PEO/PAA PEBs as a function of 1000/T [K^{-1}] for different pH values exhibits Arrhenius-like behavior $\sigma = \sigma_0 \exp(-E_a/k_B T)$ (Fig. 3b), where T is temperature and k_B the Boltzmann constant. The activation energy (E_a) determined from the Arrhenius function decreases from 0.48 eV to 0.14 eV as the solvent pH increases from 1 to 10 (Fig. 3c).

3.3. Wide-field SPR microscopy

A wide-field surface plasmon resonance microscope was employed to capture time series of 2D images. It created a spatiotemporal volume of intensities to detect the SPR effects of nano-objects and quantify their presence. The gold surface was functionalized under controlled flow conditions, and PEO/PAA-SH was deposited on the gold layer to establish connections with the analyte for detecting silica nanoparticles (Fig. 4a). The SPR sensitivity of the Au-layer and Au-(PEO/PAA-SH) layers were initially investigated through theoretical simulations using Winspall software [41]. Theoretical reflectivity curves of the Au-layer and Au-(PEO/PAA-SH) layers were plotted against the incident beam angles in Fig. 4b. The SPR angle for the Au-layer is 59.85°, which increases to 75.93° after coating with PEO/PAA PEBs. The SPR sensitivity is calculated as $S = \Delta\theta/\Delta n$, where $\Delta\theta$ represents the SPR angle shift, and Δn is the refractive index change. Consequently, a series of SPR angle values were generated by increasing the analyte's refractive index from 1.33 (refractive index of water) to 1.40, with an interval increase of 0.01 (Fig. 4c). The plot of SPR shift as a function of the analyte's refractive index displays a linear relationship, and the slope of this curve represents the SPR sensitivity. The SPR sensitivity increases from 119 deg./RIU to 178 deg./RIU when PEO/PAA PEBs are coated onto the gold layer.

Subsequently, experimental investigations are conducted using the Au-layer and Au-(PEO/PAA-SH) layers to explore the sensitivity of the wide-field surface plasmon resonance microscope (WF-SPRM) in detecting silica nanoparticles with a size of 100 nm. The study involves analyzing the signal-to-noise ratio and linewidth of the detected particles. ImageJ software is employed for image averaging and background subtraction [37]. Notably, the binding of particles to both the Au-layer and Au-PEO/PAA layers results in the sudden appearance of a distinct bright spot corresponding to the particle shape on the micrographs (as shown in the inset image of Fig. 5a).

Fig. 5a presents the time-dependent relative intensity that represents the binding event of silica nanoparticles to the sensor surface. The abrupt increase in relative intensity is indicative of a binding event. Notably, the relative intensity of the detected silica nanoparticles on the Au-(PEO/PAA-SH) layers surpasses that of the Au-layer. In Fig. 5b, the line profile in the x-direction showcases the bound silica nanoparticles on both Au- and Au-(PEO/PAA-SH) layers. The signal-to-noise ratio (S/N) for the Au-layer is 6 ± 1, which notably increases to 20 ± 1 for the Au-(PEO/PAA-SH) layers, indicating that the presence of PEO/PAA PEBs enhances the SPR sensitivity for particle detection. Moreover, the linewidth of the recorded spot decreases from 8 ± 1 pixels (Au-layer) to 5 ± 1 pixels (Au-(PEO/PAA-SH) layers), demonstrating the improved spatial resolution of the recorded images.

The second parameter that effects on detected particle intensity is the particle size, where the signal intensity of silica nanoparticle detected by the Au layer increases from about 90 a.u. to about 128 a.u. as silica nanoparticle size increases from 100 to 400 nm (Fig. 5c). On the other hand, the signal intensity of silica nanoparticle detected by the Au-(PEO/PAA-SH) layers increases from about 115 a.u. to about 165 a.u. as silica nanoparticle size increases from 100 to 400 nm (Fig. 5c). The signal intensity for silica nanoparticles detected by Au and Au-(PEO/PAA-SH) layers can be fitted by a straight line between 100 and 400 nm, indicating the fundamental difference between the Mie scattering and

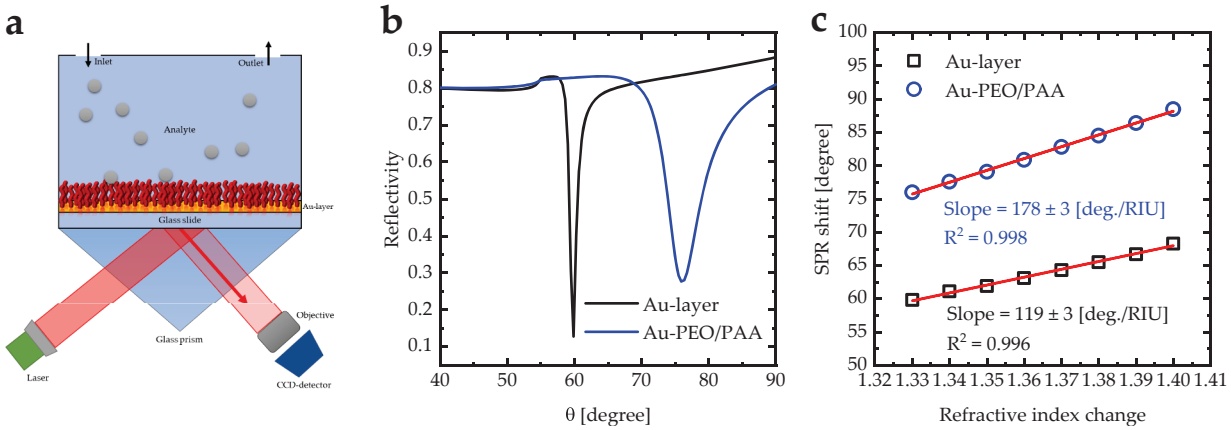

Fig. 4. **(a)** The Kretschmann configuration illustrating the prism-gold-PEO/PAA PEBs system, **(b)** Reflectivity versus incident angle for the Kretschmann configuration of the prism-gold-PEO/PAA PEBs system, and **(c)** SPR angle shift versus the refractive index change of bare Au-layer and Au-(PEO/PAA PEBs) layers.

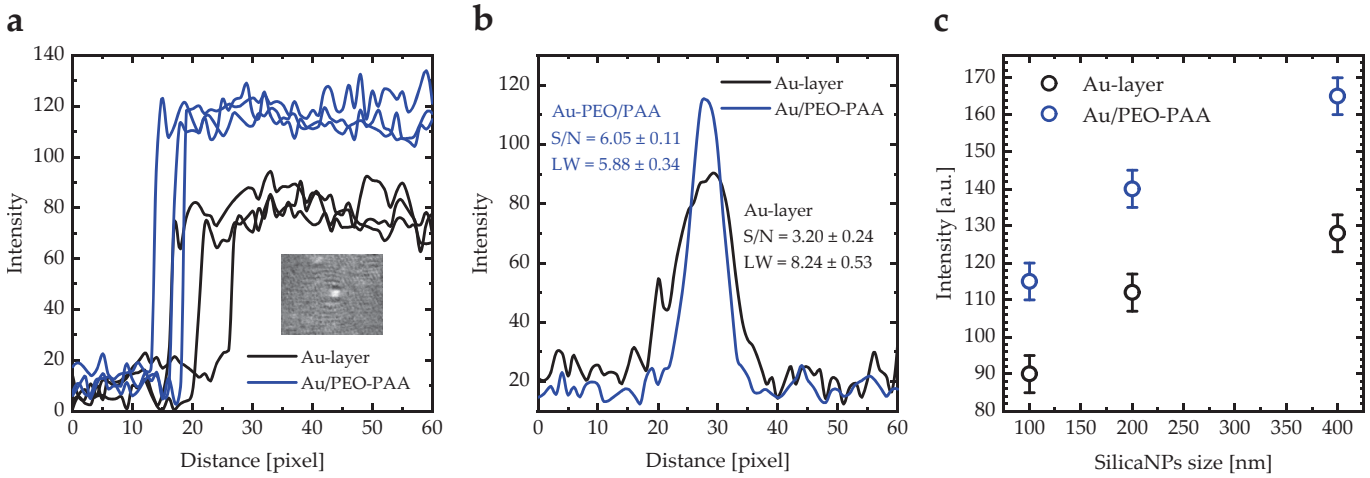

Fig. 5. **(a)** Time-dependent intensity variation in the center of the bright spot for detected silica nanoparticles using the Au-layer and Au-PEO/PAA PEBs. **(b)** Line profile plot representing the detected silica nanoparticles by the Au-layer and Au-PEO/PAA PEBs. Three independent replicates are conducted for each measurement. S/N is the signal-to-noise ratio, and LW is the linewidth. **(c)** Experimental intensity of detected silica nanoparticle by Au and Au-PEO/PAA PEBs as a function of silica nanoparticle size.

the signal-generating method. However, the dependence's regularity suggests that the images correspond to single particles rather than agglomerates.

3.4. Discrete particle detection model

The conventional mathematical model for SPR detection considers the molecules bound to the sensor surface as an effective medium with an effective refractive index and thickness [38]. The SPR image intensity of the detected silica nanoparticles is a result of the interference between the plasmons of the Au-layer and the bound molecules. This is achieved through the incident p-polarized light, which generates reflected light (E_r)) at the Au/prism interface and transmits light into the Au-layer as an evanescent wave, exciting the surface plasmons (E_{sp}) [39]. The total electric field (E) can be expressed as follows [40–42],

$$E = E_r \sin(\omega t) + E_{sp} \sin(\omega t + \varphi) \tag{1}$$

where φ is the phase shift between the background and the radiation generated by the particle. Additionally, the resulting intensity from the SPR detection process is given by [24],

$$I = c\varepsilon_0 n |E|^2 = c\varepsilon_0 n \left| E_r \sin(\omega t) + E_{sp} \sin(\omega t + \varphi) \right|^2 \tag{2}$$

or,

$$I = \frac{1}{2} c\varepsilon_0 n \left(E_r^2 + E_{sp}^2 + 2E_r E_{sp} \cos\varphi \right) \tag{3}$$

where ω is the frequency, t is time, c is the speed of light, ε_0 is the vacuum permittivity, and n is the refractive index. Moreover, the elastic scattering theory explains surface plasmon scattering by the particle, and when the surface plasmon wave is larger than the particle size, the scattered field can be expressed by a decaying cylindrical plasmonic wave [43–45],

$$E_s(r, r') = E_{sp}^0(r') e^{-\kappa |r - r'|} e^{-ik|r - r'|} \tag{4}$$

where r' is the particle location, $E_{sp}(r')$ is the SPR field in the absence of the particle, κ is the decaying constant of the SP, and k is the wave number of SPR. The total surface plasmon field (E_{sp}) based on the Born approximation is given by [44,46],

$$E_{sp}(r, r') = E_{sp}^0(r) + \alpha E_{sp}^0(r') e^{-\kappa |r - r'|} e^{-ik|r - r'|} = E_{sp}^0(r) + \alpha E_s(r, r') \tag{5}$$

where α is a scattering coefficient related to the particle's polarizability. $E_{sp}^0(r)$ is the SPR field in the absence of the particle. The SPR image contrast of the particle is described by:

$$I(r, r') = \frac{1}{2} c\varepsilon_0 n \left[\left(E_r^2 + \left(E_{sp}^0(r) + \alpha E_s(r, r') \right)^2 + 2E_r \left(E_{sp}^0(r) + \alpha E_s(r, r') \right) \cos\varphi \right) - \left(E_r^2 + E_{sp}^2 + 2E_r E_{sp} \cos\varphi \right) \right] \tag{6}$$

The system symmetry is disrupted when a molecule binds to the Au surface. A 100 nm silica nanoparticle located at 5 nm from the Au- and Au-(PEO/PAA-SH) layers is considered in the model, and the resulting electric field distribution across the structure at the resonance angle is plotted in Fig. 6a. The electric field intensity is enhanced at the metal/analyte interface at the resonance angle, breaking the symmetry of the electric field. The electric field profile at the resonance angle with the presence of silica nanoparticles was computed using COMSOL Multiphysics software. Utilizing equation (6), the intensity distribution of the binding event between the molecule and the Au- and Au-(PEO/PAA-SH) layers is calculated. Fig. 6b and 6c illustrate the intensity profile distribution for the experimentally detected silica nanoparticle bound to the Au- and Au-(PEO/PAA-SH) layers, compared with the calculated intensity profile. The agreement between the estimated intensity profile and the experimental data confirms the success of the derived model. According to the calculated and experimental results of the WF-SPRM measurements, it can be concluded that coated the Au layer by PEO/PAA-SH layer enhances the signal-to-noise ratio of the particle detection.

4. Conclusions

Polymer-polymer complexes involving polyacrylic acid (PAA) and polyethylene oxide (PEO) form hydrogen-bonding complexes, with PEO acting as the hydrogen-bond acceptor and PAA as the donor. The dissociation behavior of PEO/PAA polymer brushes is investigated under varying solvent pH conditions. At low pH values, the dominant presence of COOH groups in the PEO/PAA PEBs results in collapsed brushes due to the absence of repulsive forces between the brushes. As the pH increases to 7, the COOH groups in the top layer of the brushes dissociate into negatively charged COO^- groups, leading to the formation of swollen brushes due to electrostatic repulsion between the chains. At pH 10, all COOH groups in the PEO/PAA PEBs dissociate into negatively charged COO^- groups, further increasing electrostatic

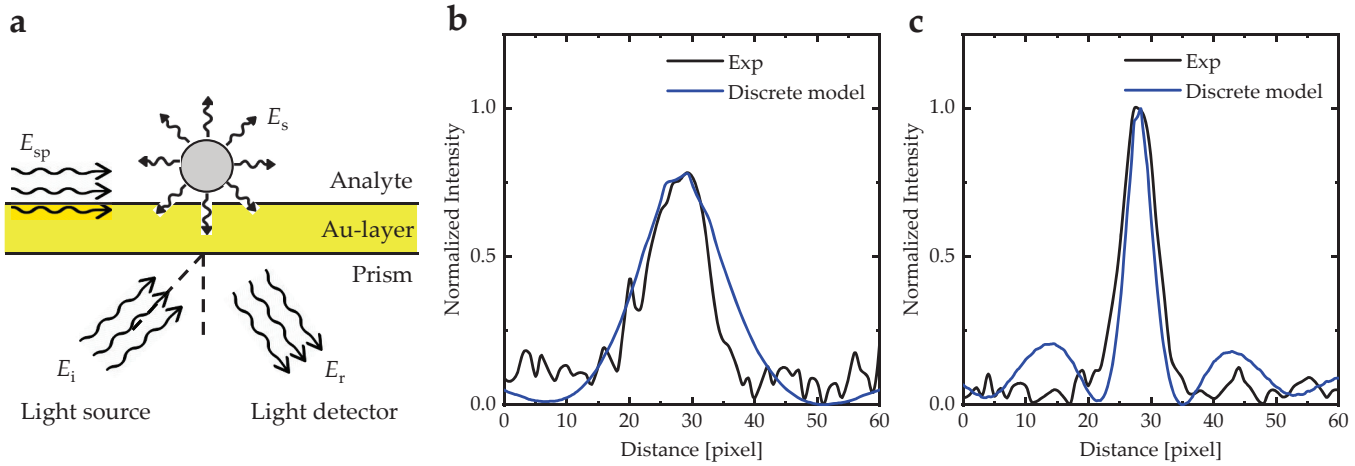

Fig. 6. Discrete Particle Model of Surface Plasmon Resonance Sensor. **(a)** Schematics illustrating the discrete particle model. Experimental and calculated intensities as a function of the distance of the silica nanoparticle from **(b)** the Au- and **(c)** the Au-(PEO/PAA-SH) layers.

repulsion and causing the brushes to stretch. With increasing pH towards 10, PEO/PAA PEBs exhibit a hydrophilic nature, promoting greater interaction with the surrounding medium. The refractive index of PEO/PAA PEBs also increases with increasing solvent pH, with the refractive index of 1.94 at 685 nm for a pH 7. The sensitivity of the wide-field surface plasmon resonance microscope (WF-SPRM) is explored through theoretical and experimental approaches using an Au-(PEO/PAA PEBs) layer. The theoretical sensitivity of the Au-(PEO/PAA PEBs) layer improves from 118.5 deg./RIU to 178.1 deg./RIU compared to the Au-layer. Moreover, the signal-to-noise ratio for the Au-(PEO/PAA PEBs) layer increases from 6 ± 1 to 20 ± 1 compared to the Au layer. Following this, a mathematical model to describe discrete particle detection by WF-SPRM is presented. The calculated intensity profile derived from the model matches well with the experimental data, confirming the validity of this approach.

Funding

This research received no external funding.

CRediT authorship contribution statement

Qais M. Al-Bataineh: Writing – original draft, Visualization, Software, Methodology, Formal analysis, Data curation, Conceptualization. **Ahmad D. Telfah:** Writing – original draft, Visualization, Validation, Supervision, Resources, Project administration, Methodology, Investigation, Conceptualization. **Carlos J. Tavares:** Writing – review & editing, Visualization, Validation, Formal analysis. **Roland Hergenröder:** Writing – review & editing, Validation, Supervision, Software, Resources, Project administration, Investigation, Data curation.

Declaration of competing interest

The authors declare that they have no known competing financial interests or personal relationships that could have appeared to influence the work reported in this paper.

Data availability

Data will be made available on request.

Acknowledgments

The scientific support by the Ministerium für Innovation, Wissenschaft und Forschung des Landes Nordrhein-Westfalen, the Senatsverwaltung für Wirtschaft, Technologie und Forschung des Landes Berlin, and the Bundesministerium für Bildung und Forschung is gratefully acknowledged. We also thank Prof. Ahmad A. Ahmad for helping our members use the thin films laboratory at Jordan University of Science and Technology.

Appendix A. Supplementary data

Supplementary data to this article can be found online at https://doi.org/10.1016/j.apsusc.2023.159189.

References

[1] S. Zou, R. Lv, Z. Tong, B. Na, K. Fu, H. Liu, In situ hydrogen-bonding complex mediated shape memory behavior of PAA/PEO blends, Polymer 183 (2019), 121878.
[2] A. Khaldi, J.A. Elliott, S.K. Smoukov, Electro-mechanical actuator with muscle memory, J. Mater. Chem. C 2 (38) (2014) 8029–8034.
[3] A. Ahmad, et al., Synthesis and characterization of ZnO NPs-doped PMMA-BDK-MR polymer-coated thin films with UV curing for optical data storage applications, Polym. Bull. 78 (3) (2021) 1189–1211.
[4] Q.M. Al-Bataineh, A.A. Ahmad, A.M. Alsaad, A. Telfah, New Insight on photoisomerization kinetics of photo-switchable thin films based on azobenzene/graphene hybrid additives in polyethylene oxide, Polymers 12 (12) (2020) 2954.
[5] J. Kunzelman, T. Chung, P.T. Mather, C. Weder, Shape memory polymers with built-in threshold temperature sensors, J. Mater. Chem. 18 (10) (2008) 1082–1086.
[6] J. Hao, G. Yuan, W. He, H. Cheng, C.C. Han, C. Wu, Interchain Hydrogen-Bonding-Induced Association of Poly (acrylic acid)-graft-poly (ethylene oxide) in Water, Macromolecules 43 (4) (2010) 2002–2008.
[7] Y. Wang, E.J. Goethals, F.E. Du Prez, Association Behavior between End-Functionalized Block Copolymers PEO-PPO-PEO and Poly (acrylic acid), Macromol. Chem. Phys. 205 (13) (2004) 1774–1781.
[8] H. Kaczmarek, A. Szalla, H. Chaberska, J. Kowalonek, Changes of surface morphology in UV-irradiated poly (acrylic acid)/poly (ethylene oxide) blends, Surf. Sci. 566 (2004) 560–565.
[9] R.-Y. Wang, et al., Closed-loop phase behavior of block copolymers in the presence of competitive hydrogen-bonding and Coulombic interaction, Macromolecules 51 (12) (2018) 4727–4734.
[10] G. Liu, X. Ding, Y. Cao, Z. Zheng, Y. Peng, Shape memory of hydrogen-bonded polymer network/poly (ethylene glycol) complexes, Macromolecules 37 (6) (2004) 2228–2232.
[11] T. Liu, J. Li, Y. Pan, Z. Zheng, X. Ding, Y. Peng, A new approach to shape memory polymer: design and preparation of poly (methyl methacrylate) composites in the presence of star poly (ethylene glycol), Soft Matter 7 (5) (2011) 1641–1643.
[12] J. Yuan, H.S. Antila, E. Luijten, Dielectric effects on ion transport in polyelectrolyte brushes, ACS Macro Lett. 8 (2) (2019) 183–187.
[13] E. Currie, A. Sieval, G. Fleer, M.C. Stuart, Polyacrylic acid brushes: surface pressure and salt-induced swelling, Langmuir 16 (22) (2000) 8324–8333.
[14] J. Yuan, H.S. Antila, E. Luijten, Structure of polyelectrolyte brushes on polarizable substrates, Macromolecules 53 (8) (2020) 2983–2990.
[15] S. Das, M. Banik, G. Chen, S. Sinha, R. Mukherjee, Polyelectrolyte brushes: theory, modelling, synthesis and applications, Soft Matter 11 (44) (2015) 8550–8583.

[16] G. Ferrand-Drake del Castillo, R.L. Hailes, A. Dahlin, Large Changes in Protonation of Weak Polyelectrolyte Brushes with Salt Concentration—Implications for Protein Immobilization, J. Phys. Chem. Lett. 11 (13) (2020) 5212–5218.
[17] M. Delcroix, et al., Design of mixed PEO/PAA brushes with switchable properties toward protein adsorption, Biomacromolecules 14 (1) (2013) 215–225.
[18] M. Delcroix, S. Demoustier-Champagne, C.C. Dupont-Gillain, Quartz crystal microbalance study of ionic strength and pH-dependent polymer conformation and protein adsorption/desorption on PAA, PEO, and mixed PEO/PAA brushes, Langmuir 30 (1) (2014) 268–277.
[19] A. Bratek-Skicki, P. Eloy, M. Morga, C. Dupont-Gillain, Reversible Protein adsorption on mixed PEO/PAA Polymer brushes: Role of Ionic strength and PEO content, Langmuir 34 (9) (2018) 3037–3048.
[20] M. Ballauff, O. Borisov, Polyelectrolyte brushes, Curr. Opin. Colloid Interface Sci. 11 (6) (2006) 316–323.
[21] C. Yigit, M. Kanduc, M. Ballauff, J. Dzubiella, Interaction of charged patchy protein models with like-charged polyelectrolyte brushes, Langmuir 33 (1) (2017) 417–427.
[22] M. Koenig, et al., Adsorption of enzymes to stimuli-responsive polymer brushes: Influence of brush conformation on adsorbed amount and biocatalytic activity, Colloids Surf. B Biointerfaces 146 (2016) 737–745.
[23] W.M. De Vos, F.A. Leermakers, A. De Keizer, M.A. Cohen Stuart, J.M. Kleijn, Field theoretical analysis of driving forces for the uptake of proteins by like-charged polyelectrolyte brushes: effects of charge regulation and patchiness, Langmuir 26 (1) (2010) 249–259.
[24] A. Zybin, V. Shpacovitch, J. Skolnik, R. Hergenröder, Optimal conditions for SPR-imaging of nano-objects, Sens. Actuators B 239 (2017) 338–342.
[25] H.K. Rouf, T. Haque, Performance enhancement of Ag-Au bimetallic surface plasmon resonance biosensor using InP, Progr. Electromagnetics Res. M 76 (2018) 31–42.
[26] V. Shpacovitch, et al., Application of the PAMONO-sensor for quantification of microvesicles and determination of nano-particle size distribution, Sensors 17 (2) (2017) 244.
[27] A. Shalabney, I. Abdulhalim, Sensitivity-enhancement methods for surface plasmon sensors, Laser Photonics Rev. 5 (4) (2011) 571–606.
[28] Q.M. Al-Bataineh, A.D. Telfah, V. Shpacovitch, C.J. Tavares, R. Hergenröder, Switchable Polyacrylic Acid Polyelectrolyte Brushes for Surface Plasmon Resonance Applications, Sensors 23 (9) (2023) 4283.
[29] A. Ahmad, A. Migdadi, A. Alsaad, Q.M. Al-Bataineh, A. Telfah, Optical, structural, and morphological characterizations of synthesized (Cd–Ni) co-doped ZnO thin films, Appl. Phys. A 127 (12) (2021) 1–12.
[30] A. Alsaad, Q.M. Al-Bataineh, A. Ahmad, Z. Albataineh, A. Telfah, Optical band gap and refractive index dispersion parameters of boron-doped ZnO thin films: A novel derived mathematical model from the experimental transmission spectra, Optik 211 (2020), 164641.
[31] Q.M. Al-Bataineh, V. Shpacovitch, D. Sadiq, A. Telfah, R. Hergenröder, Surface Plasmon Resonance Sensitivity Enhancement Based on Protonated Polyaniline Films Doped by Aluminum Nitrate, Biosensors 12 (12) (2022) 1122.
[32] A.W. Peterson, M. Halter, A. Tona, A.L. Plant, High resolution surface plasmon resonance imaging for single cells, BMC Cell Biol. 15 (1) (2014) 1–14.
[33] D. Aulich, et al., In situ studies on the switching behavior of ultrathin poly (acrylic acid) polyelectrolyte brushes in different aqueous environments, Langmuir 26 (15) (2010) 12926–12932.
[34] R. Dong, M. Lindau, C.K. Ober, Dissociation behavior of weak polyelectrolyte brushes on a planar surface, Langmuir 25 (8) (2009) 4774–4779.
[35] P. Pillai, P. Khurana, A. Tripathi, Dielectric studies of poly (methyl methacrylate)/polystyrene double layer system, J. Mater. Sci. Lett. 5 (6) (1986) 629–632.
[36] M.A. AL-Akhras, S.E. Alzoubi, A.A. Ahmad, R. Ababneh, A. Telfah, Studies of composite films of polyethylene oxide doped with potassium hexachloroplatinate, J. Appl. Polym. Sci. 138 (5) (2021) 49757.
[37] W.S. Rasband. "ImageJ." National Institutes of Health. https://imagej.nih.gov/ij/ (accessed).
[38] J. Maurya, Y. Prajapati, V. Singh, J. Saini, R. Tripathi, Performance of graphene–MoS 2 based surface plasmon resonance sensor using silicon layer, Opt. Quant. Electron. 47 (11) (2015) 3599–3611.
[39] H. Yu, X. Shan, S. Wang, H. Chen, N. Tao, Molecular scale origin of surface plasmon resonance biosensors, Anal. Chem. 86 (18) (2014) 8992–8997.
[40] H. Raether, Surface plasmons on gratings, Surface plasmons on smooth and rough surfaces and on gratings, 1988, pp. 91-116.
[41] T. Leskova, A. Maradudin, W. Zierau, Surface plasmon polariton propagation near an index step, Opt. Commun. 249 (1–3) (2005) 23–35.
[42] S.-H. Cao, W.-P. Cai, Q. Liu, Y.-Q. Li, Surface plasmon–coupled emission: what can directional fluorescence bring to the analytical sciences? Annu. Rev. Anal. Chem. 5 (2012) 317–336.
[43] B. Hecht, H. Bielefeldt, L. Novotny, Y. Inouye, D. Pohl, Local excitation, scattering, and interference of surface plasmons, Phys. Rev. Lett. 77 (9) (1996) 1889.
[44] S.I. Bozhevolnyi, V. Coello, Elastic scattering of surface plasmon polaritons: modeling and experiment, Phys. Rev. B 58 (16) (1998) 10899.
[45] A. Shchegrov, I. Novikov, A. Maradudin, Scattering of surface plasmon polaritons by a circularly symmetric surface defect, Phys. Rev. Lett. 78 (22) (1997) 4269.
[46] S.I. Bozhevolnyi, Localization phenomena in elastic surface-polariton scattering caused by surface roughness, Phys. Rev. B 54 (11) (1996) 8177.